AIP | Journal of Applied Physics

Pyroelectric-field driven defects diffusion along c-axis in ZnO nanobelts under high-energy electron beam irradiation

Yong Ding, Ying Liu, Simiao Niu, Wenzhuo Wu, and Zhong Lin Wang

Citation: Journal of Applied Physics **116**, 154304 (2014); doi: 10.1063/1.4898644
View online: http://dx.doi.org/10.1063/1.4898644
View Table of Contents: http://scitation.aip.org/content/aip/journal/jap/116/15?ver=pdfcov
Published by the AIP Publishing

Pyroelectric-field driven defects diffusion along *c*-axis in ZnO nanobelts under high-energy electron beam irradiation

Yong Ding,[a] Ying Liu, Simiao Niu, Wenzhuo Wu, and Zhong Lin Wang
School of Materials Science and Engineering, Georgia Institute of Technology, Atlanta, Georgia 30332-0245, USA

(Received 25 August 2014; accepted 7 October 2014; published online 17 October 2014)

When ZnO nanobelts are exposed to a high-dose electron probe of several nanometers to hundred nanometers in diameter inside a transmission electron microscope, due to the radiolysis effect, part of oxygen atoms will be ejected into the vacuum and leaving a Zn-ion rich surface with a pit appearance at both the electron-entrance and electron-exit surfaces. At the same time, a temperature distribution is created around the electron probe due to local beam heating effect, which generates a unidirectional pyroelectric field. This pyroelectric field is strong enough to drive Zn ions moving along its positive *c*-axis direction as interstitial ions. In the first case, for the ZnO nanobelts with *c*-axis lie in their large surfaces, defects due to the aggregation of Zn interstitial ions will be formed at some distances of 30–50 nm approximately along the *c*-axis direction from the electron beam illuminated area. Alternatively, for the ZnO nanobelts with ±(0001) planes as their large surfaces, the incident electron beam is along its *c*-axis and the generated pyroelectric field will drive the interstitial Zn-ions to aggregate at the Zn terminated (0001) surface where the local electrical potential is the lowest. Such electron beam induced damage in ZnO nanostructures is suggested as a result of Zn ion diffusion driven by the temperature gradient induced pyroelectric field along *c*-axis. Our study shows a radiation damage caused by electron beam in transmission electron microscopy, especially when the electron energy is high. © *2014 AIP Publishing LLC*.
[http://dx.doi.org/10.1063/1.4898644]

I. INTRODUCTION

ZnO is one of the most important materials in materials research today. ZnO nanobelts/nanowires have attracted worldwide attention because of important applications in LEDs, biomedical devices, solar cells, electronics, nanogenerators, piezotronics, and piezo-phototronics.[1–11] From a structural point of view, ZnO has a non-central symmetric wurtzite crystal structure, which naturally produces a piezoelectric polarization when the material is strained.[8] In addition to strain, a change in temperature can also produce polarization, known as pyroelectricity and quantitatively defined by the pyroelectric coefficient $P_3 = \Delta P/\Delta T$, where ΔP and ΔT are the changes of polarization and temperature, respectively.[12] Such temperature sensitized pyroelectric properties have been extensively utilized in fabricating inexpensive room-temperature infrared detectors.[13] Recently, using ZnO nanowires, pyroelectric nanogenerators for harvesting pyroelectric energy have been successfully demonstrated.[14,15]

The microscopic origin of pyroelectricity in ZnO is related to the temperature-gradient induced polarization owing to the non-central symmetric Wurtzite structure.[12,16] Experimentally, the pyroelectric coefficient is the sum of the primary coefficient and the secondary coefficient.[12,13,17] The primary pyroelectric coefficient describes the polarization produced when the dimensions and volume of the crystal are held fixed under a change in temperature. This is commonly called the strain-free case. If the crystal is allowed to change its dimensions and volume during the temperature change, in another word, stress-free case, strain will be induced due to thermal expansion, resulting in an additional contribution of piezoelectric polarization. Such polarization change of piezoelectric origin is described as a secondary pyroelectric coefficient. In this work, ZnO nanobelts were heated up locally by a focused nanometer-sized high-energy electron beam inside a transmission electron microscope (TEM). We can assume the region far away from the electron beam has no temperature change. Therefore, the heated region will be contained by the surrounding cooled area. Therefore, such pyroelectric field can be classified to the strain-free case, or the primary pyroelectric one.

In order to reveal such pyroelectric field in ZnO nanobelts triggered by electron beam heating effect, we need to investigate the interaction between the high-energy electron beam and ZnO nanobelts first. It is well-known that the electron beam used in a TEM not only provides useful structural and chemical information but also cause temporary or permanent change/damage at the surface or in bulk structure of specimen.[17–19] Such radiation damages include heating, electrostatic charging, ionization damage (radiolysis), sputtering, atomic displacement, etc. With a 100 keV electron-beam irradiated on II–V compounds, the local temperature can increase as high as ~210 °C.[20–22] A positively charged nanocolumn will form within the insulating material under electron irradiation.[23–25] In the case of transition-metal oxides, ionization damage or radiolysis is believed to occur via the Knotek-Feibelman mechanism: the incident electron creates an inner-shell vacancy on the metal site followed by

[a]Electronic mail: yong.ding@mse.gatech.edu

interatomic Auger decay from the oxygen.[26–28] This results in a neutral or positive oxygen atom that is repelled by the surrounding metal ions and ejected into vacuum, leaving a metal-rich surface with a pitted appearance. If the electron-beam has a high dose and is illuminated for a long time, a hole may be drilled in the specimen.[29–34]

In this work, due to the radiolysis effect, oxygen atoms located close to surfaces will be ejected into the vacuum and leaving a Zn-ion rich (Zn^{+} and/or Zn^{2+}) column with two pits at both the electron-entrance and electron-exit surfaces. With elongation of illumination time, holes were drilled through the ZnO nanobelts. The local temperature increase due to the electron beam heating effect generates the unidirectional pyroelectric field. The relatively lower electrical potential is located at its positive *c*-axis direction of the electron beam irradiated area. Such pyroelectric field will drive the Zn-ions toward the positive *c*-axis of the nanobelt as interstitial ions. The interstitial Zn-ions will stop at the surface where the *c*-axis is perpendicular to the nanobelt surface, or some distance (30–50 nm) away from the electron-beam illuminated area where the *c*-axis is inside the nanobelt surface, and aggregate to form a defect structure. The formation and distribution of the defects reveal the pyroelectric field triggered by the electron-beam heating effect.

II. EXPERIMENTAL DETAILS

The ZnO nanobelts were synthesized using the vapor deposition approach.[3] A FEI Tecnai F30 super-twin field-emission-gun TEM equipped with a single-tilt tomography holder from Fischione Instrument was used to acquire the TEM images, select-area electron diffraction (SAED), convergent-beam electron diffraction (CBED) patterns, and high-angle annular dark-field (HAADF) scanning transmission electron microscopy (STEM) images. The TEM was operated at 300 kV. By varying the spot size and focusing condition, the diameters of the electron beam irradiated on ZnO nanobelts were adjusted from several nanometers to hundred nanometers with beam-dose change from $3 \times 10^7 A/m^2$ to $1 \times 10^5 A/m^2$. The spot size 9 was used to acquire the CBED patterns and HAADF STEM images with a reduced beam-dose close to $1 \times 10^4 A/m^2$. JEMS software from Dr. Stadelmann was used to do the CBED simulation. COMSOL software was used to calculate the temperature, pyroelectric field, and electrical potential distribution within the ZnO nanobelts.

III. RESULTS AND DISCUSSION

Figure 1(a) shows a TEM bright-field image from a ZnO nanobelt before being damaged by the high-dose electron

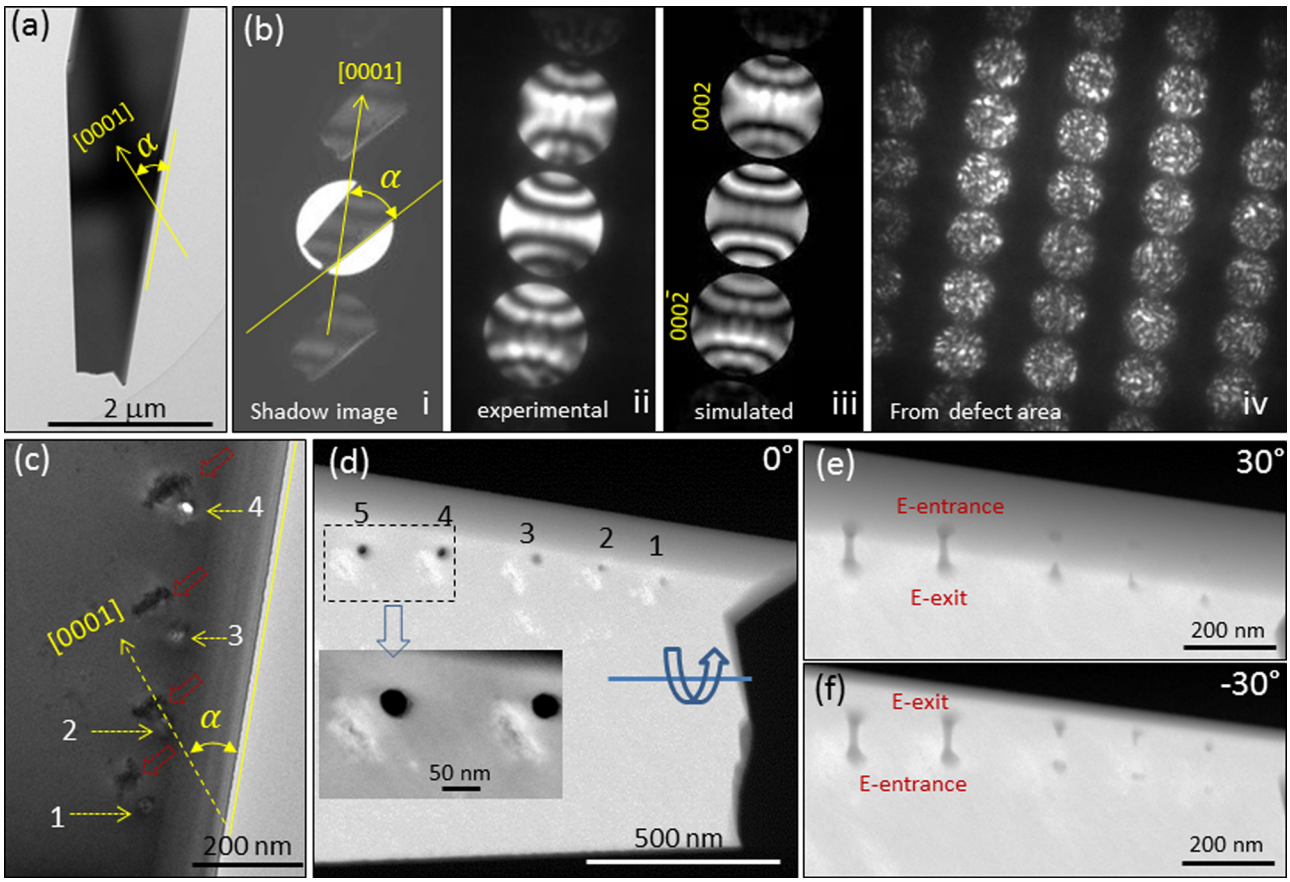

FIG. 1. (a) A low-magnification bright-field TEM image to show a ZnO nanobelt with no electron beam damage yet. (b-i) A shadow image from the nanobelt in (a). (b-ii) and (b-iii) are experimental and simulated CBED pattern. (b-iv) CBED pattern recorded from the defects area in (c). (c) A TEM image shows the electron irradiation induced pits, holes, and defects. (d) A HAADF STEM image from the same area as shown in (c). (e) and (f) give the HAADF STEM image form the ZnO nanobelt after tilting along the horizontal axis by 30° and −30°, respectively. E-entrance and E-exit mark the electron entrance and electron exit surfaces, respectively.

beam. The *c*-axis of the nanobelt can be identified by its shadow-image [Fig. 1(b-i)] combined with the CBED pattern [Fig. 1(b-ii)].[35] The incident electron beam is identified as along the $[01\bar{1}0]$ direction of the Wurtzite structure. In order to identify the positive *c*-axis in the CBED pattern, JEMS software was used to do the CBED simulation. The best matched simulation result is displayed in Fig. 1(b-iii) corresponding to the sample thickness ~178 nm. The confirmed positive *c*-axis is highlighted by yellow arrowheads in both TEM images and CBED pattern in Fig. 1.

Using spot-size 3 and focusing the electron beam to ~5 nm in radius with a beam dose close to $1 \times 10^6 A/m^2$ to illuminate the ZnO nanobelts in 1, 2, and 3 min separately, we can get pits marked 1, 2, and 3 in Fig. 1(c), respectively. By increasing the dose to $3 \times 10^7 A/m^2$ by switching the spot-size to 1, we can drill hole 4 in 2 min. We observed extra defect contrast 30–50 nm away from each pit/hole as marked by the red arrowheads in Fig. 1(c). We can confirm that during the pits and holes formation period, no electron beam was irradiated on the defects area. The CBED pattern from a defect area was recorded and displayed in Fig. 1(b-iv). No extra diffraction spot was observed in the CBED pattern. Therefore, no new phase nucleated in these areas. The complex contrast in the diffraction disks may come from thickness changes and/or local strain field. An interesting phenomenon is that if we link the pit/hole to the middle of the related defect, such direction always points along the positive *c*-axis of the nanobelt.

Figure 1(d) gives a HAADF STEM image of the same nanobelt as shown in Fig. 1(c). The inset gives the enlarged image from the dashed rectangle enclosed area. The defects give brighter contrast in the HAADF STEM images. Therefore, we assume more Zn-ions in the defects areas. However, our x-ray energy dispersive spectra (XEDS) did not give us clear evidence due to the limited resolution. By tilting the sample positive and negative 30° along a horizontal axis, the projected HAADF STEM images are displayed in Figs. 1(e) and 1(f), respectively. After precise determination of the geometrical relationship between the nanobelt and the tilting axis of the TEM holder, we can determine that the electron-entrance surface is towards the top in the 30° tilted image, Fig. 1(e) and the electron-exit surface is towards the bottom, reversed in the negative 30° tilted image, Fig. 1(f). Based on the tilted images, we can see that pits formed at both electron-entrance and electron-exit surfaces at the early period of the electron-beam irradiation. As time passed, the pit at the electron-exit surface grew faster compared with the one at the electron-entrance surface. When the two pits meet each other, a hole has been drilled. By measuring the distance between the pits at electron-entrance and electron-exit surfaces in Fig. 1(e) or Fig. 1(f), we can get the ZnO nanobelt thickness as 190 ± 10 nm, which is pretty close to the result calculated from CBED simulation.

Because the pits and holes in Fig. 1 are close to the side surface of the nanobelts, the asymmetry formation of the defects around the pits and holes may be affected by the side surface. In order to rule out such possibility, we focused the electron beam on the middle part and another side of the same nanobelt to check whether the defects formed in the same way. Figure 2(a) gives a TEM bright-field image to show more pits and holes formed in another side of the same

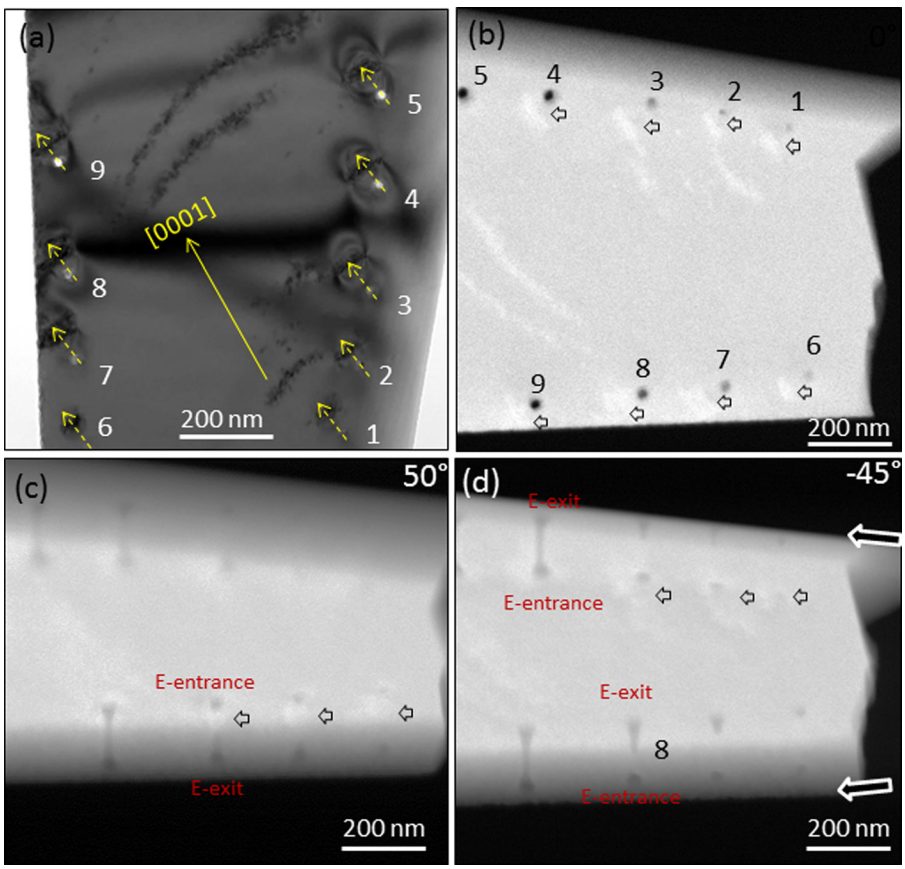

FIG. 2. (a) A bright-field TEM image after 4° tilting to show clear strain field around each defect. (b), (c), and (d) give the HAADF STEM images from the same nanobelt in (a) with no tilt and 50° and −45° tilts, respectively.

nanobelt as well. By small angle (4°) tilting, the local strain field around the defects can be seen more clearly in Fig. 2(a). Without exception, the direction from the pit/hole to the center of the defect is always pointed along the positive *c*-axis of the nanobelt. All of the defects give brighter contrast in HAADF STEM images compared to the defect-free area of the nanobelt. By tilting the nanobelt along the horizontal axis 50° and −45°, respectively, we recorded another two HAADF STEM images as displayed in Figs. 2(c) and 2(d). The defects contrast seems to be located close to the electron-entrance surface, and away from the electron-exit surface as marked by the white arrowheads.

When we spread the electron beam to hundred nanometers scale, after several minutes, an arc shaped defect formed outside the electron-beam irradiated area as displayed in Fig. 3(a). Similarly, the direction from the center of the beam to the center of the defect is pointed along the positive *c*-axis. Such defects in arc shape were observed in Fig. 2 as well, which are formed during the high-resolution TEM (HRTEM) image recording with big electron beam size. In order to identify whether the defect is located on the surface or in the body of the nanobelt, a series of tilting HAADF STEM images were recorded in Figs. 3(c)–3(f). Two pits were made as markers of the electron-entrance and electron-exit surfaces, which are pointed by a dark arrowhead in Figs. 3(b) and 3(c). By tilting the nanobelt along the horizontal axis, we find the projected distance between the defect and the pit at the electron-entrance surface shrinks, and the extended defect contrast moves towards the pit at the electron-exit surface. Therefore, we can conclude that the defect is close to the electron-entrance surface and extends inside the nanobelt, but does not reach the electron-exit surface. The inserted drawing in Fig. 3(b) outlines the distribution of defects inside the nanobelt.

We classify the defect as an aggregation of dislocation loops, which is formed by the aggregation of interstitial Zn-ions. The evidence is given in Fig. 4. Due to the ionization effect or the radiolysis, oxygen atoms will be ejected from the electron beam irradiated area to leave Zn-ion rich surfaces. The charge states of Zn ion can be +1 or +2. Considering the high mobility of Zn interstitials,[36] it is reasonable to link the defect with the extra Zn ions. The CBED pattern from the defect area still belongs to the wurzite structure, therefore, no new phase formed. At the area close to the arc shaped defect, we can find some separated small defects as shown in Fig. 4. We can record the migration of defects even under a comparable weak electron-beam. For example, the defect in the middle of Fig 4(a) migrated ∼10 nm in 18 s to the location shown in Fig. 4(b). It can be considered as interstitial Zn-ions moving under local thermal or electric potential perturbation. A HRTEM image from a small defect is displayed in Fig. 4(c), giving "black-white" diffraction contrast, the same contrast as the dislocation loops.[37] With more defects aggregated together, its mobility may drop. In some cases, the defects can be dissolved under electron beam irradiation as displayed in Figs. 4(d) to 4(f). It can be considered as the segregation of the aggregated interstitial Zn-ions.

Then what is the driving force to move such interstitial Zn-ions to locations outside the electron beam irradiated area? This force is unidirectional along the positive *c*-axis. As mentioned in the Introduction,[23,24] a positive charge will build up during the electron beam irradiation as the result of secondary and Auger electron emission. However, the

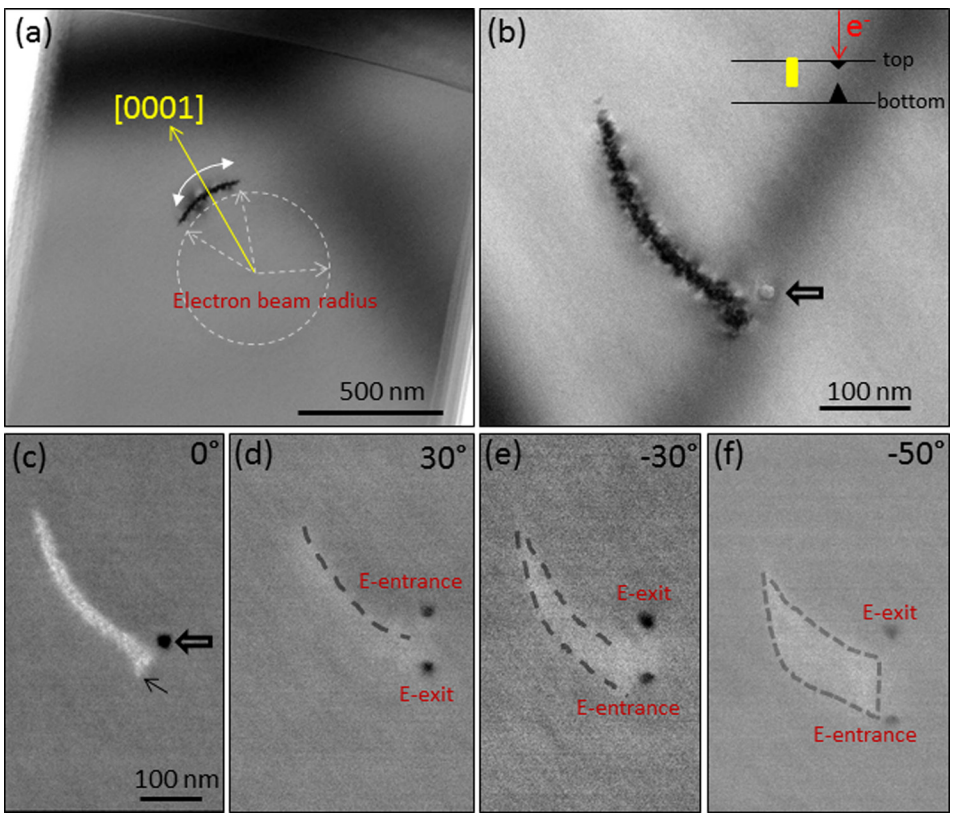

FIG. 3. (a) A bright-field TEM image to show the arc shaped defect formed due to electron beam irradiation with beam radius around 250 nm. (b) Magnified TEM image to show both the arc shaped defect and the pit formed by small electron beam irradiation with radius around 10 nm. (c)-(f) HAADF STEM images corresponding to tilting the sample around the horizontal axis by 0°, 30°, −30°, and −50°, respectively.

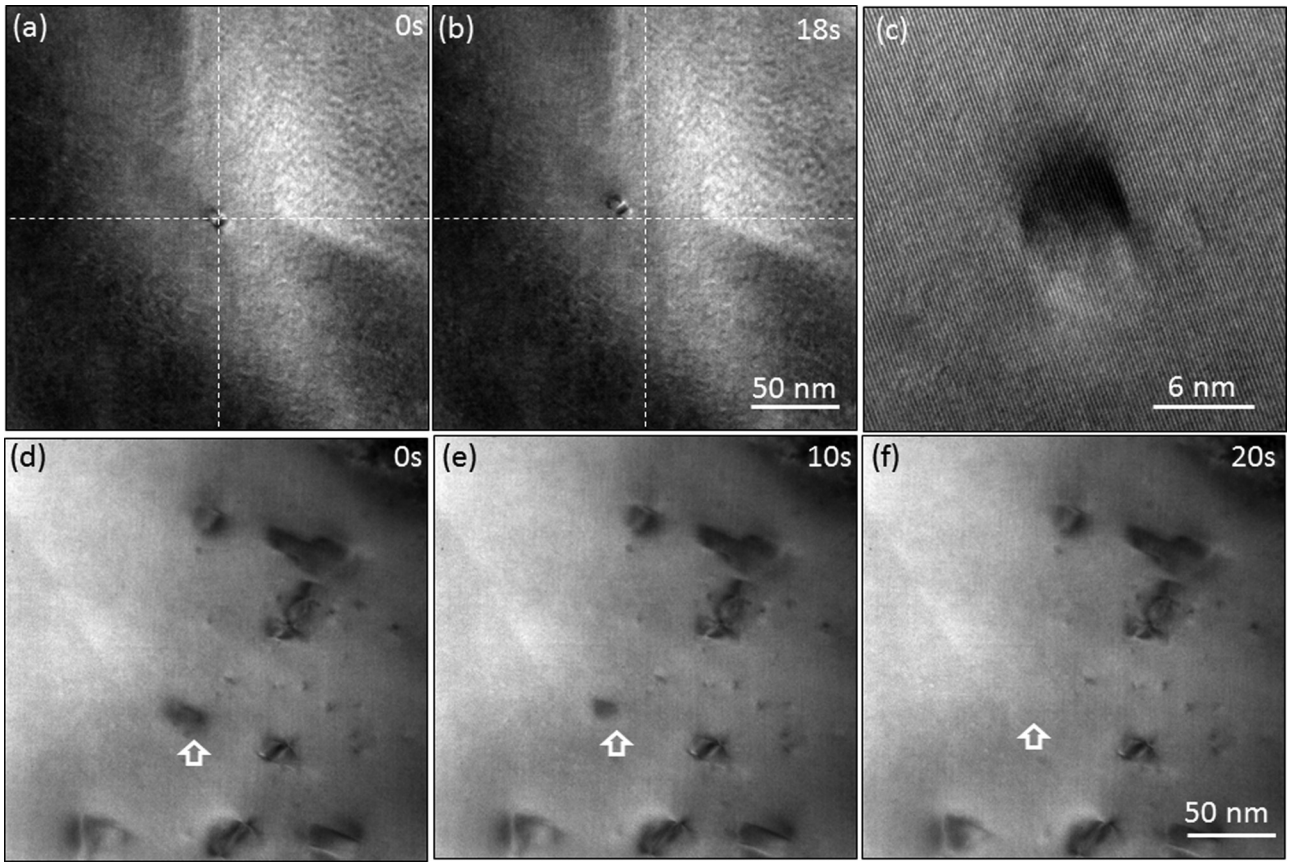

FIG. 4. (a) and (b) Two TEM images from a defect recorded with 18 s interval to show the mobility of the defect. (c) A HRTEM image from a tiny defect. (d)-(f) give three TEM images from a same area with 10 s interval.

electric field from the positive charges should be symmetrical around the irradiated area. If the positive charges create an electric force, which serves as the driving force, the defects will form a closed loop instead of small arc. This conflicts with our experimental results. Another possibility is the temperature gradient related thermoelectric effect, for such temperature gradient doses exist around the electron probe illuminated area due to the electron beam heating effect. The temperature increases due to the electron beam heating is material dependent. In the literature, the calculated temperature increase of II-V compounds under a 100 keV electron beam varies from 16.3 to 123 °C.[20] ZnO has a closer packed structure compared to ZnS due to the lighter anion in the compound. It should have a similar temperature increase as that of ZnS, which is predicted as 123 °C and measured <210 °C.[20] At the atomic scale, an applied temperature gradient causes charge carriers in the material to diffuse from the hot side to the cold side; such uneven distribution of charges creates a thermoelectric field.[38] Considering the symmetrical temperature distribution around the electron probe in ZnO nanobelts, the resulted thermoelectric field will be symmetric as well. Therefore, the thermoelectric effect cannot be the main driving force for the formation of the defects as discussed above.

Considering the force is along the *c*-axis, therefore, it must be polarization related electric force. The static polarization of ZnO nanobelts is usually cancelled by the stray charges from its environment. The strain field around the defects will produce piezoelectric polarization. However, such piezoelectric polarization is the result of the formation of the defects, not the driving force to form the defects. Considering the electron beam heating effect, it is possible to create a pyroelectric field triggered by the local temperature change resulting from the electron beam heating. And further, such temperature change is location dependent. Considering the pyroelectric coefficient P_3 of ZnO is $\sim -9.4 \mu Cm^2K^{-1}$ and the room-temperature (T_r) polarization as zero, the polarization at an increased temperature (T) will be $P(T) = P_3 \times (T - T_r) < 0$.[39] Increased temperature will generate a polarization towards the negative *c*-axis direction. Therefore, the electrical potential at the positive *c*-axis direction is lower than that at the negative *c*-axis direction, and an electric field towards positive *c*-axis direction will be generated.

Figure 5(a) gives the calculated temperature distribution due to the heating effect from the electron beam focused on the small circle. The positive *c*-axis is defined as pointing upward. A 30 °C increase in temperature was assumed in the calculation. The pyroelectric potential simulation utilized the Heat Transfer module and Partial Differential Equation module of COMSOL Multiphysics. A round shaped electron beam with radius of 10 nm is placed in the center of the 1 μm × 1 μm ZnO surface and set as a fixed temperature heat source. The electrical potential is calculated through integration of polarization, and polarization is calculated by the pyroelectric equation: $dP = p_3 dT$. The calculated electrical

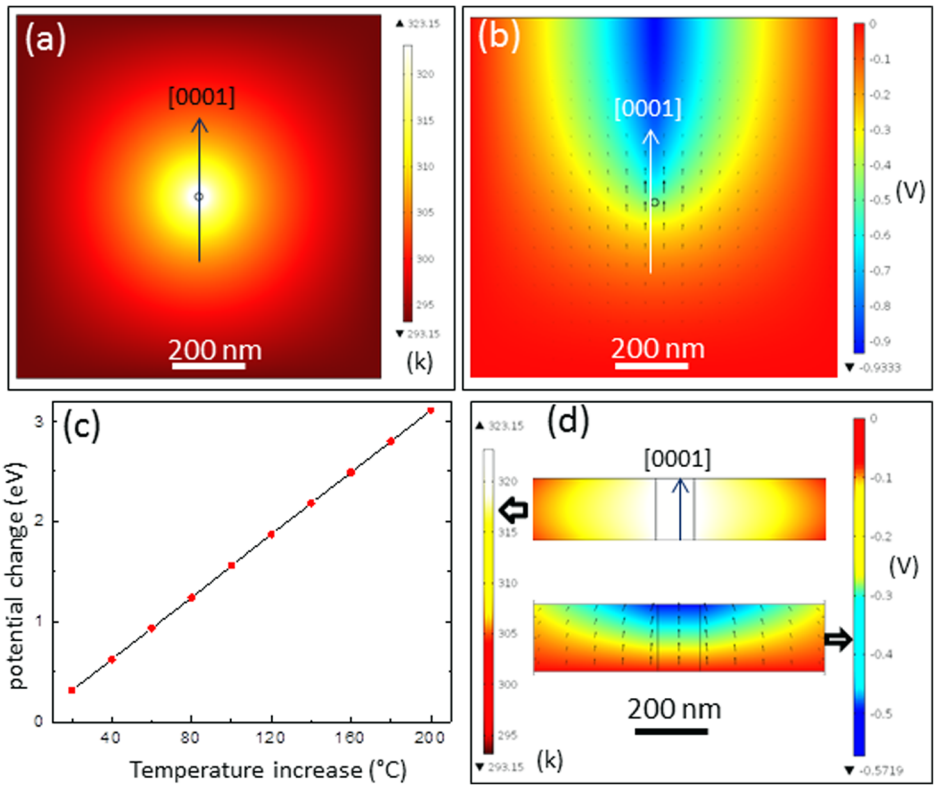

FIG. 5. (a) Calculated temperature distribution in a ZnO nanobelt, the center circle corresponds to the area where the electron beam is focused on. (b) Electrical potential (color) and pyroelectric field (arrowheads) distribution caused by the temperature change as illustrated in (a). (c) Electrical potential changes in (b) from the center to the top with different temperature increases. (d) The temperature, electrical potential, and pyroelectric field distributions as the case in (a) and (b), the difference is that the c-axis is perpendicular to the nanobelt surface, while the case in (a) and (b) is parallel.

potential distribution is put in Fig. 5(b), and the arrowheads inserted give the electric field orientation. The longer arrowhead indicates a stronger local electric field. We notice that the strongest pyroelectric field is at the electron probe area, and as the distance from the probe area increases, the pyroelectric field drops. There must be a location where the pyroelectric field is not strong enough to drive the Zn ions further. Experimentally, this distance is 30–50 nm away from the probe area as displayed in Fig. 1. The relationship between the temperature change and the electrical energy gained by an interstitial Zn-ion (Zn^+) after moving from the beam irradiation area (the center) to the low potential area (the top center) is drawn in Fig. 5(c). Even with 30 °C temperature increases, the Zn-ion can gain 0 .466 eV of energy. Considering the migration barrier of Zn interstitial as suggested from 0 .22 eV for Zn^+ to 0 .57 eV for Zn^{2+},[36,40–42] the pyroelectric field is strong enough to drive the Zn interstitial ions to move away from the electron beam irradiated area. The orientation will be along the positive *c*-axis of the ZnO nanobelts.

When the temperature stabilized, i.e., $\Delta T = 0$, there will be no more pyroelectric field. In reality, the formation of the defect starts at the beginning of the high-dose beam irradiation. Even in 1 or 2 s after focusing the nanometer sized electron probe on the ZnO nanobelt, then quickly spreading the beam to lower the dose, we observed defect formation. Longer time exposure to high-dose electron beam will expel more oxygen ions into vacuum and generate more interstitial

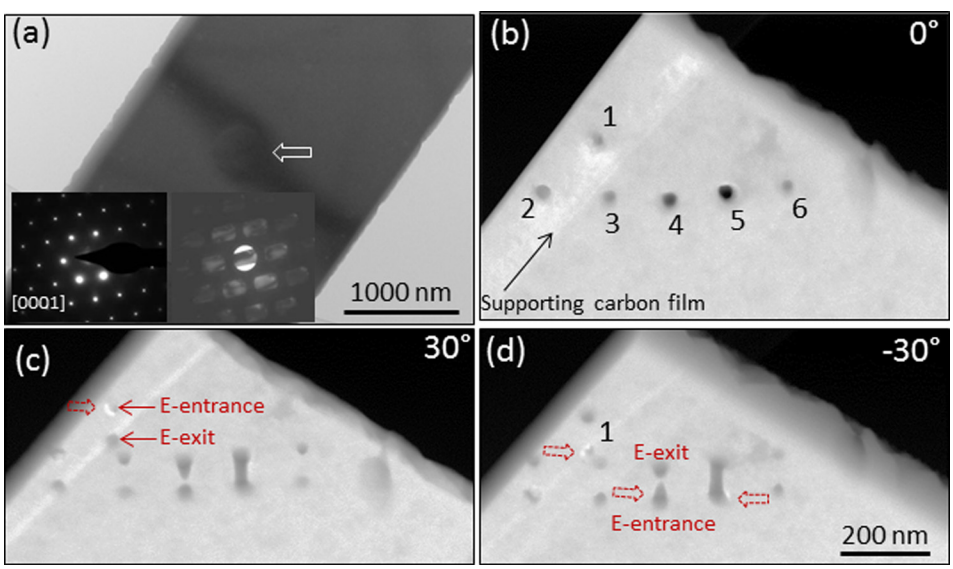

FIG. 6. (a) A bright-field TEM image from a ZnO nanobelt with its c-axis perpendicular to its large surface, the insets are the SAED pattern and shadow image. (b)-(d) The HAADF STEM images from one end of the nanobelt in (a) at different tilting angles of 0°, 30°, and −30°, respectively.

Zn ions. The defects can grow larger before the pyroelectric field disappears.

Alternatively, if the *c*-axis of the ZnO nanobelt is perpendicular to its large surface, the electron beam direction is parallel to the *c*-axis, then the temperature increase generated pyroelectric field and potential distribution will look like the case as displayed in Fig. 5(d). If the positive *c*-axis is pointing upward, the pyroelectric field will drive the Zn-ion upward to aggregate at the top surface or the electron-entrance surface. The ZnO nanobelt in Fig. 6 belongs to such case. The SAED pattern and shadow image from the nanobelt is inserted in Fig. 6(a). The incident electron beam is parallel to the *c*-axis and the growth direction of the nanobelt is along the $[01\bar{1}0]$ direction. A big pit with radius around 200 nm pointed by a white arrowhead was formed after electron beam irradiation. No arc shaped defect like that in Fig. 3 is observed. Figure 6(b) shows the pits and holes drilled at one end of the ZnO nanobelt, which are indexed from 1 to 6. After tilting along the horizontal axis by $\pm 30°$, we can separate the pits located at the electron-entrance and electron-exit surfaces clearly in Figs. 6(c) and 6(d). A brighter contrast can be identified in the pits located at the electron-entrance surface as marked by hollow red arrowheads in both Figs. 6(c) and 6(d). It indicates that the same kind of defects formed inside the pits, unlike the case in Figs. 1 and 2 which are away from the pits. In both cases with *c*-axis parallel or perpendicular to its surface, the formation of defects is driven by the pyroelectric field as illustrated in Fig. 5.

IV. CONCLUSION

When a high-energy electron beam irradiated on ZnO nanobelts, the local temperature increase due to the electron beam heating effect will generate a pyroelectric field. At the same time, due to the radiolysis, oxygen atoms are repelled from the irradiated area and leave Zn-ion rich surfaces. The pyroelectric field is strong enough to drive the interstitial Zn-ions to move from high potential to low potential area, corresponding to along the positive *c*-axis direction. The aggregated Zn-ions form dislocation loop like defects. The pyroelectric field distribution inside ZnO nanobelts outlines the location of the defects. Furthermore, the defects also point out the positive *c*-axis direction simultaneously. Our study reveals a process of defect generation by electron beam for studying of nanomaterials.

ACKNOWLEDGMENTS

This work was supported by the Hightower chair foundation. The authors thank Ken C. Pradel for his assistance in manuscript writing.

[1]P. Fei, P. H. Yeh, J. Zhou, S. Xu, Y. F. Gao, J. H. Song, Y. D. Gu, Y. Y. Huang, and Z. L. Wang, Nano Lett. **9**, 3435 (2009).
[2]D. Kaelblein, R. T. Weitz, H. J. Bottcher, F. Ante, U. Zschieschang, K. Kern, and H. Klauk, Nano Lett. **11**, 5309 (2011).
[3]Z. W. Pan, Z. R. Dai, and Z. L. Wang, Science **291**, 1947 (2001).
[4]J. I. Sohn, S. S. Choi, S. M. Morris, J. S. Bendall, H. J. Coles, W. K. Hong, G. Jo, T. Lee, and M. E. Welland, Nano Lett. **10**, 4316 (2010).
[5]X. D. Wang, J. Zhou, J. H. Song, J. Liu, N. S. Xu, and Z. L. Wang, Nano Lett. **6**, 2768 (2006).
[6]Z. L. Wang, MRS Bull. **32**, 109 (2007).
[7]Z. L. Wang, J. Phys. Chem. Lett. **1**, 1388 (2010).
[8]Z. L. Wang and J. H. Song, Science **312**, 242 (2006).
[9]J. Zhou, P. Fei, Y. D. Gu, W. J. Mai, Y. F. Gao, R. Yang, G. Bao, and Z. L. Wang, Nano Lett. **8**, 3973 (2008).
[10]Y. F. Hu, Y. L. Chang, P. Fei, R. L. Snyder, and Z. L. Wang, ACS Nano **4**, 1234 (2010).
[11]X. N. Wen, W. Z. Wu, and Z. L. Wang, Nano Energy **2**, 1093 (2013).
[12]J. Albertsson, S. C. Abrahams, and A. Kvick, Acta Crystallogr., Sect. B: Struct. Sci., Cryst. Eng. Mater. **45**, 34 (1989).
[13]C. P. Ye, T. Tamagawa, and D. L. Polla, J. Appl. Phys. **70**, 5538 (1991).
[14]Y. Yang, W. X. Guo, K. C. Pradel, G. Zhu, Y. S. Zhou, Y. Zhang, Y. F. Hu, L. Lin, and Z. L. Wang, Nano Lett. **12**, 2833 (2012).
[15]Y. Yang, K. C. Pradel, Q. S. Jing, J. M. Wu, F. Zhang, Y. S. Zhou, Y. Zhang, and Z. L. Wang, ACS Nano **6**, 6984 (2012).
[16]G. Donnay, Can. Mineral. **23**, 655 (1985).
[17]R. F. Egerton, R. McLeod, F. Wang, and M. Malac, Ultramicroscopy **110**, 991 (2010).
[18]R. F. Egerton, P. Li, and M. Malac, Micron **35**, 399 (2004).
[19]R. F. Egerton, Microsc. Res. Tech. **75**, 1550 (2012).
[20]Y. Y. Loginov, P. D. Brown, and N. Thompson, Phys. Status Solidi A **126**, 63 (1991).
[21]Y. M. Xu, L. A. Shi, X. T. Zhang, K. W. Wong, and Q. Li, Micron **42**, 290 (2011).
[22]K. A. Mkhoyan and J. Silcox, Appl. Phys. Lett. **82**, 859 (2003).
[23]J. Cazaux, Ultramicroscopy **60**, 411 (1995).
[24]N. Jiang, J. Phys. D: Appl. Phys. **46**, 305502 (2013).
[25]T. Yamamoto, T. Hirayama, K. Fukunaga, and Y. Ikuhara, Nanotechnology **15**, 1324 (2004).
[26]M. R. Mccartney, P. A. Crozier, J. K. Weiss, and D. J. Smith, Vacuum **42**, 301 (1991).
[27]D. E. Diaz-Droguett, A. Zuniga, G. Solorzano, and V. M. Fuenzalida, J. Nanopart. Res. **14**, 679 (2012).
[28]M. R. Mccartney and D. J. Smith, Surf. Sci. **250**, 169 (1991).
[29]T. J. Bullough, Philos. Mag. A **75**, 69 (1997).
[30]N. Jiang and J. C. H. Spence, Ultramicroscopy **113**, 77 (2012).
[31]D. G. Howitt, S. J. Chen, B. C. Gierhart, R. L. Smith, and S. D. Collins, J. Appl. Phys. **103**, 024310 (2008).
[32]H. M. Kim, M. H. Lee, and K. B. Kim, Nanotechnology **22**, 275303 (2011).
[33]S. Tehuacanero-Cuapa, R. Palomino-Merino, and J. Reyes-Gasga, Radiat. Phys. Chem. **87**, 59 (2013).
[34]G. S. Chen and C. J. Humphreys, J. Appl. Phys. **85**, 148 (1999).
[35]Y. Ding and Z. L. Wang, J. Phys. Chem. B **108**, 12280 (2004).
[36]P. Erhart and K. Albe, Appl. Phys. Lett. **88**, 201918 (2006).
[37]K. Arakawa, M. Hatanaka, E. Kuramoto, K. Ono, and H. Mori, Phys. Rev. Lett. **96**, 125506 (2006).
[38]D. M. Rowe, *Thermoelectrics Handbook: Macro to Nano* (Taylor & Francis, 2006).
[39]T. B. Bateman, J. Appl. Phys. **33**, 3309 (1962).
[40]F. Oba, M. Choi, A. Togo, and I. Tanaka, Sci. Technol. Adv. Mater. **12**, 034302 (2011).
[41]A. Janotti and C. G. Van de Walle, J. Cryst. Growth **287**, 58 (2006).
[42]A. Janotti and C. G. Van de Walle, Phys. Rev. B **76**, 165202 (2007).